

Agentic Additive Manufacturing Alloy Evaluation

Peter Pak,[†] Achuth Chandrasekhar,[†] and Amir Barati Farimani^{*,†,‡}

[†] *Department of Mechanical Engineering, Carnegie Mellon University, Pittsburgh, PA, USA*

[‡] *Machine Learning Department, Carnegie Mellon University, Pittsburgh, PA, USA*

E-mail: barati@cmu.edu

Abstract

Agentic systems enable the intelligent use of research tooling, augmenting a researcher’s ability to investigate and propose novel solutions to existing problems. Within Additive Manufacturing (AM), alloy selection and evaluation remains a complex challenge, often requiring expertise in the various domains of materials science, thermodynamic simulations, and experimental analysis. Large Language Model (LLM) enabled agents can facilitate this endeavor by utilizing their extensive knowledge base to dispatch tool calls via Model Context Protocol (MCP) to perform actions such as thermo-physical property diagram calculations and lack of fusion process map generation. In addition, the multi-agent system can effectively reason through complex user prompts and provide analysis on the lack of fusion process window of common alloys such as SS316L and IN718 along with proposed composition variants of known alloys. These agents can dynamically adjust their task trajectory to the outcomes of tool call results, effectively enabling autonomous decision-making in practical environments. This work aims to showcase the benefits of adopting a LLM enabled multi-agent system to automate and accelerate the task of evaluating proposed additive manufacturing alloys, both novel and known.

1 Introduction

Evaluation of an alloy’s suitability for fabrication and its appropriate processing parameters is a key component of the Additive Manufacturing (AM) process. In industries that focus on biomedical, aerospace, or energy challenges, their unique applications often involve the selection and evaluation of alloy candidates that are best equipped to perform in their service environment.¹⁻⁶ In addition, considerations such as deformation,⁷⁻⁹ corrosion resistance,^{1,10} and biocompatibility¹¹⁻¹³ are key motivators for composition refinement which can foster the development of novel alloys. However, the discovery and validation of new AM alloys remains a time-consuming process that often requires expertise in materials science, computational simulations, and experimental analysis.^{2,4,5} Furthermore, each alloy presents its own set of unique challenges, often requiring specific build parameters to avoid potential defects within part fabrication.^{2,14-21} The search and optimization of desirable process parameters often requires extensive simulation analysis and experimental trials to validate their suitability within build conditions.^{8,22-25}

For the task of obtaining material properties for a novel elemental composition, Computer Calculation of Phase Diagrams²⁶ (CALPHAD) is commonly performed to calculate the individual phases of an alloy via Gibbs Free Energy and numerical optimization. CALPHAD provides a rigorous thermodynamic framework for predicting equilibrium phase stability and composition in multicomponent alloys by combining assessed Gibbs energy descriptions of individual phases with numerical minimization of the total free energy. In practice, modern CALPHAD workflows go beyond phase fields, as well-curated mobility and property databases enable the prediction of temperature-dependent thermophysical quantities such as thermal conductivity (k), specific heat capacity (C_p), and density (ρ).^{27,28} An estimation of material properties for a proposed alloy composition is predicted with this method using a library of resources to obtain relevant information regarding various elements, alloys, and application properties.

With the procurement of the material properties of a proposed alloy composition, its

suitability for an AM build is assessed through numerical solvers. Solvers such as those developed by Eagar-Tsai²⁹ and Rosenthal³⁰ provide preliminary information on the temperature field of a melt pool through an analytical solution. Whereas, OpenFOAM³¹ and FLOW-3D³² utilize Computational Fluid Dynamics (CFD) to provide a more detailed analysis of the underlying fluid flow, heat transfer, and solidification phenomena of the melt pool.^{33,34} The obtained melt pool dimensions are used to calculate potential defect regimes within a process map of beam power and scanning velocity combinations.^{23,35,36} Specifically, the lack of fusion defect region is of primary concern as insufficient melting induces the formation of large pores and in extreme cases can cause the build process to fail.²³ Insight into this defect regime is essential for the informed selection of optimal build parameters within the process window.

Recent advances in multi-agent systems have demonstrated the potential of Large Language Models (LLMs) to perform complex, goal-oriented tasks that extend beyond the constraints of a single prompt.³⁷⁻⁴⁴ This has been applied to the monitoring and adjustment of real-time Fuse Deposition Modeling (FDM) builds,³⁷ search and discovery of potential catalyst and drug candidates,^{38,39} and optimization of material and molecular design simulations.^{40,43} In these tasks, LLMs autonomously determine the next course of action by reasoning over the information available within the dynamic environment.^{37,39,40} The next course of action often involves utilizing functionality external to the LLM which is made accessible through a tool call. This can be done through various methods and solution providers include LangChain⁴⁵ and LlamaIndex.⁴⁶ This work utilizes the Model Context Protocol (MCP)⁴⁷ as the library for creating and exposing tools for the LLM that allow seamless integration into any client with an MCP interface.

With these established goals, this work aims to develop a multi-agent system for the search, proposal, and analysis of novel alloy compositions suitable for additive manufacturing. The inclusion of the LLM allows for the intelligent automation and reasoning of tool generated responses from natural language inputs which can be constructed into valid func-

tion inputs. MCP tool binding from `thermo-calc` and `additive-manufacturing` packages allow for the actions such as process map generation and material property prediction to be controlled by agents. The multi-agent system is able to reason and plan through given tasks and dynamically adjust task trajectories based on tool responses. This in turn enables the intelligent automation of routine tasks and accelerates the evaluation of novel alloy compositions within additive manufacturing.

2 Methodology

2.1 Calculation of Thermophysical Properties

For this task, given an hypothetical element composition of a specific alloy, Thermo-Calc⁴⁸ is expected to provide the relevant material properties of density, thermal conductivity, specific heat capacity, electric resistivity, and the liquidus and solidus phase transition temperatures. Thermo-Calc utilizes a CALPHAD based solver to calculate equilibrium phase diagrams and extrapolate properties along with the material property databases to assist with obtaining thermophysical properties for various alloys. The platform also includes their TC-Python SDK allowing for programmatic use of the features, providing an interface for the creation and binding of agentic tools callable via MCP.

With the Thermo-Calc’s property diagram calculation function, a composition of elements is provided to generate a property diagram to extract material properties. Compositions consist of the mass fraction of individual elements and for commonplace alloys, a map of their elemental compositions is obtained from existing literature sources.^{15–19,25,49–57} In this process, a suitable database (one of TCFE14, TCNI12, TCAL9, TCTI6, and TCHEA7, or PURE5⁵⁸) is selected to obtain the necessary phase and transport properties with the appropriate SI units. Database selection is determined through matching an alloy’s primary element composition to its database counterpart. The element with the highest weight fraction is designated as the ”top” element. A composition is deemed as multi-principal if at least

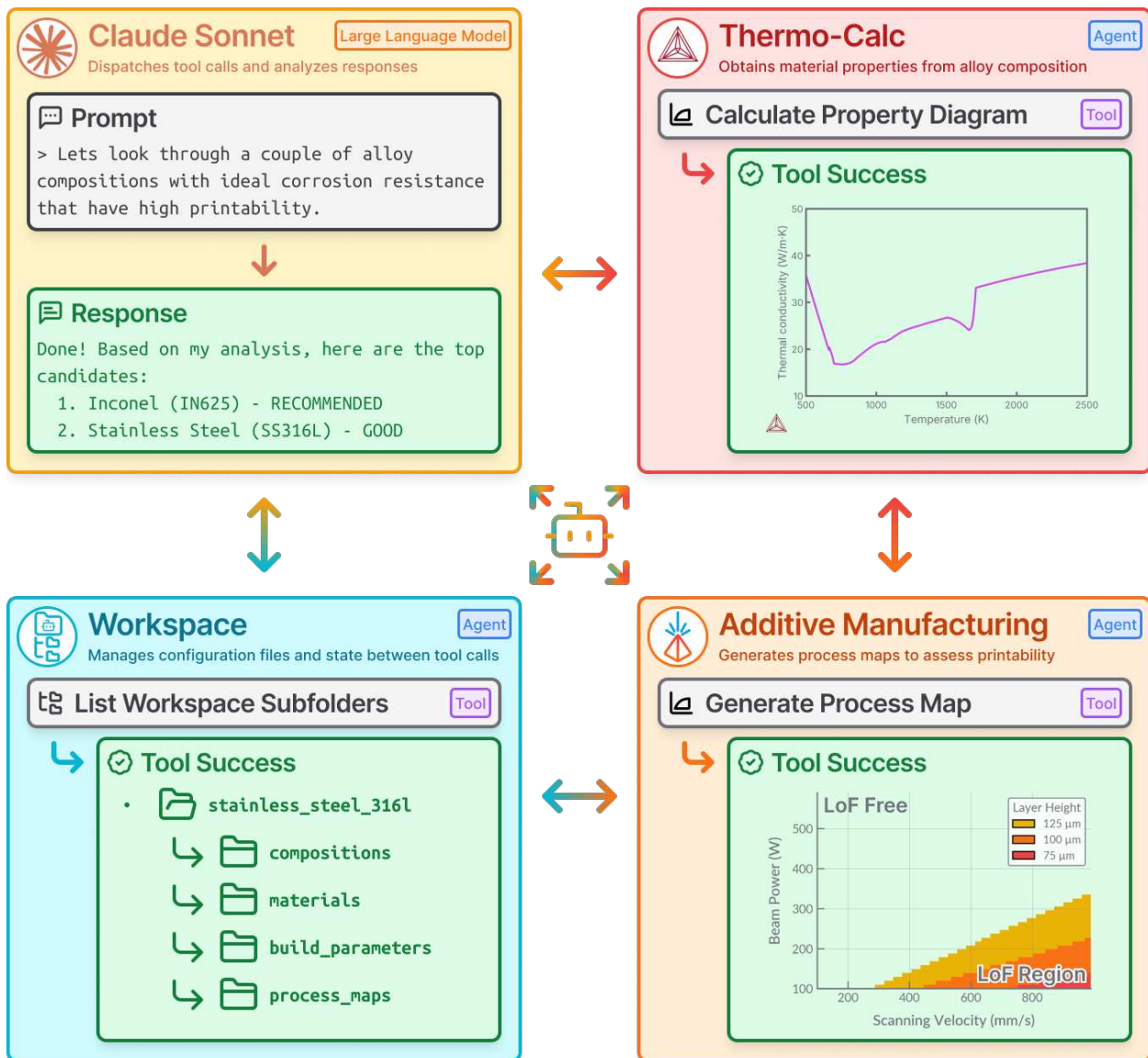


Figure 1: **(Top Left)** An input query for alloy compositions regarding the printability of an additively manufactured part suitable for its intended use case is provided to Claude Sonnet. This Large Language Model (LLM) calls the tools necessary to generate and analyze each potential alloy compositions, providing a response of candidates ranked by their content of their lack of fusion fusion regimes. **(Top Right)** Thermo-Calc allows for the retrieval of material properties for an hypothetical alloy composition, for instance thermal conductivity, to be used in down stream lack of fusion calculations. **(Bottom Left)** Workspaces provide a way for each of the tools to effectively communicate with one another and handles state management and file organization. **(Bottom Right)** Tools managed by the Additive Manufacturing subagents then utilize the calculated material properties from the Thermo-Calc subagent to generate a lack of fusion process map to send back to the LLM for analysis and final recommendation.

three elements have individual weight fractions ≥ 0.15 . Then the appropriate database is selected by elimination in the order as described in Appendix C. The provided compositions and database values are then utilized in equilibrium calculations where the minimization of Gibbs Free Energy is iteratively calculated until convergence is met.^{59,60}

Solidus and liquidus phase transition temperatures are extrapolated through tracking the liquid volume fraction. A one-dimensional temperature sweep is performed to find a point where the liquid fraction moves from approximately 0 to 1. The default arguments for the minimum and maximum temperature ranges are 500 K and 3500 K respectively. The obtained solidus and liquidus temperatures are utilized in subsequent tasks to obtain material properties from the proposed alloy. Density ($\rho = B/V$) and specific heat capacity are obtained through Thermo-Calc's user function using the ratio of mass (B) to volume (V) and the temperature derivative of molar enthalpy denoted as `HM.T` respectively. Thermal conductivity and electrical resistivity are built-in thermodynamic quantities and can be readily obtained at a given temperature. The melting temperature is taken as the average between the solid and liquidus phases.

The calculated material properties of absorptivity, thermal conductivity, liquidus and solidus phase transition temperatures, density, and specific heat capacity are saved as a common material configuration compatible with the `additive-manufacturing` package. These values will then be utilized with the tools there for initialization and generation of a lack of fusion process map to evaluate the printing feasibility of these material properties.

The accuracy of the material properties thus obtained, are highly dependent on the coverage and fidelity of the Thermo-Calc databases used. For complex alloy chemistries, such as multi-principal element alloys the software may have to interpolate between sparse input data points or extrapolate beyond them. Moreover, the present study does not utilize independently calibrated models and the quantitative accuracy is determined by good agreement with literature trends. All of these factors may introduce some uncertainty in the final predictions.

2.1.1 Absorptivity Calculation and Limitation

Absorptivity is approximated using the series expansion for emissivity in a direction normal to the surface, based on Drude's Theory (Equation 1).⁶¹ Here, $\varepsilon_\lambda(T)$ denotes the emissivity at a given wavelength (λ) and temperature (T) where the conductivity of a metal (γ) is expected in units of $(\Omega \cdot \text{cm})^{-1}$.

$$\varepsilon_\lambda(T) = \frac{0.365}{\sqrt{\gamma\lambda}} - \frac{0.0667}{\gamma\lambda} + \frac{0.006}{\sqrt{(\gamma\lambda)^3}} - \dots \quad (1)$$

Since resistivity (ρ) and conductivity (γ) are reciprocal properties ($\gamma = \frac{1}{\rho}$), Equation 1 can be modified to accept our computed electrical resistivity value and near infrared wavelength of 1070 nm. (Equation 2).

$$\varepsilon_\lambda(T) = 0.365\sqrt{\frac{\rho}{\lambda}} - 0.0667\frac{\rho}{\lambda} + 0.006\sqrt{\left(\frac{\rho}{\lambda}\right)^3} - \dots \quad (2)$$

This approximation provides a simple estimation of a given alloy's absorptivity and serves a baseline value to use with melt pool calculations. A more comprehensive approach would include the absorptivity value's dependence to applied power and the reflections observed within a melt pool during keyholing.^{62,63} For alloys such as copper which exhibits a large range of absorptivity values (around 5% to 90%)⁶³ depending on power and laser conditions, the predicted results may be limited by the stated assumptions. Our approach is validated by comparison with experimental data in Appendix D.⁶⁴⁻⁶⁷

2.2 Lack of Fusion Defect Prediction

Defects created within the laser powder bed fusion process can arise through various means and affect the final part's material and mechanical properties.^{35,68,69} This includes defects such as porosity, microstructural inhomogeneity, and inclusions which can result in degraded performance in fatigue life as well as mechanical strength.^{68,70} The source of these defects

can be attributed to at least one of the following process map defect regimes of either Lack of Fusion (LoF), Keyholing, or Balling.^{36,68} Of these defects, porosity lack of fusion porosity is often larger than that generated by keyholing or balling.⁷¹ Pores presents a significant risk to the fatigue life as it provides a starting point for cracks to nucleate from.^{70,72}

The criterion for lack of fusion is primarily concerned with overlap between subsequent melt pool tracks, where adjustments to the hatch spacing along with layer height determine the extent of unfused powder within the scan track.^{23,68} This is modeled by with Equation 3^{23,68,73} where computed ratios greater than 1 are expected to exhibit lack of fusion defects.

$$\left(\frac{\text{Hatch Spacing}}{\text{Melt Pool Width}} \right)^2 + \left(\frac{\text{Layer Height}}{\text{Melt Pool Depth}} \right)^2 \leq 1 \quad (3)$$

Hatch spacing and layer height are independent process parameters that are prescribed for the build process. Melt pool dimensions of depth and width are physical values that obtained from either cross-sectional measurements of the scan track⁷⁴ or modeling using solvers such as that of the Rosenthal^{23,24,30} equation (Equation 5).

2.2.1 Dimensional Approximation of the Melt Pool

In Equation 5, the local temperature T (K) is obtained at a distance z (m) along the travel direction for a radial distance R (m) from the beam position.^{24,30} Additional factors such as the temperature of the plate T_∞ (K), applied power Q (W), scan speed V (m/s), thermal diffusivity α (m²/s), and thermal conductivity k (W/mK) utilized to provide an approximate calculation of the temperature field.^{24,30} Thermal diffusivity ($\alpha = \frac{k}{\rho C_p}$) can be obtained from thermal conductivity k (W/mK), density ρ (kg/m³), and specific heat capacity C_p (J/kg·K). Radial distance R is the combined coordinate of $R^2 = z^2 + r^2$ where z (also $-\xi$) is the distance along the center line.

$$z = R + \frac{2\alpha}{V} \ln \left(\frac{2\pi k R \Delta T}{\epsilon P} \right) \quad (4)$$

Given the liquidus temperature of a material, Equation 5 can be rearranged to provide the bounds of the melt pool. This is shown with Equation 4, where $\Delta T = T_{melting} - T_{initial}$ and ϵ represents the dimensionless absorptivity value. The length of the melt pool can be obtained by calculating the length of the temperature field in front and tailing the heat source. The tailing length (Equation 15) of the heat source can be obtained from setting the z to R and then solving for R as seen with its derivation included in Appendix B. This provides a stop point when passing R values into Equation 4 with a step size of 1 μm when calculating the bounds, recording the maximum to use as the melt pool dimensions.

$$T = T_{\infty} + \frac{Q}{2\pi kR} \exp\left(\frac{V(z - R)}{2\alpha}\right) \quad (5)$$

2.2.2 Model Assumptions and Limitations

With Rosenthal's approximation of a moving heat source a number of assumptions are made which include a melt pool in conduction mode, a point heat source, and temperature-independent thermal properties.^{23,30} The derived melt pool dimensions are limited to a steady state conduction mode melt pool and when applied to the lack of fusion criterion it does not consider dimensional fluctuations of the melt pool that are present in experimental builds.⁷⁵

Since these melt pool dynamics are obtained through a purely conduction based approach, factors such as keyholing are not reflected in the obtained dimensions throughout the process map. When viewed through the lens of defects pertaining to lack of fusion, these dimensions present more conservative estimates to the process window. This is from the smaller depth estimations of the melt pool in conduction mode as to that of a keyholing melt pool which has an elongated lower half.^{68,70,76} Lack of fusion and keyhole defect regimes do have some degree of overlap however experimental data shows this occurs in combinations of low to medium power and low velocity ranges (Figure 12). Energy density can be used as an indicator for the transition between keyhole and conduction mode and for alloys with known energy density transition points, this value is used as a cutoff for conduction based melt pool dimensional

approximations.⁷⁰

2.2.3 Defect Domain Scope and Applicability

Although this work primarily focuses upon the prediction of lack of fusion defects within a range of power and velocity combinations, it is worth addressing the other two common defect regimes of keyholing and balling.

Keyholing describes the elongated depth of the melt pool as it exits conduction mode, leading to potential defects that can also contribute to lower mechanical strength in the resulting build.⁷⁰ A common criterion for keyholing analyzes the width to depth ratio of the melt pool such that a melt pool with a depth 1.5 larger than the width is considered to be keyholing (Equation 6).⁷⁷

$$\frac{Width}{Depth} > 1.5 \quad (6)$$

However, in order to properly model keyhole behavior within the melt pool, a computational fluid dynamics approach is required to capture effects such as solid/liquid interfaces and the driving force of recoil pressure from material vaporization.⁷⁸ Solvers from FLOW-3D³² and OpenFOAM³¹ provide the capability to model these fluid dynamics but present a non-trivial challenge to integrate into this agentic system as they require both significant time and computational cost.

Balling presents another potential source of defects which often occurs at high power and velocity combinations, the grooves generated from the capillary forces initiate voids within the build if not remelted in a subsequent pass.⁷⁹ A simplification of the criterion for balling is comparing the length to width ratio of the melt pool to a set threshold, such as π , such that any ratio greater would indicate balling⁷⁷ (Equation 7).

$$\frac{Length}{Width} < \pi \quad (7)$$

For the case of balling, a threshold based on the ratio length and width of the melt pool is rather simplistic and presents an assumption that this behavior occurs based on the dimensions of the melt pool. Whereas, factors such as the temperature balance between the melt pool and the solid surface provides a more grounded approach to capturing the underlying behaviors that would contribute to balling phenomenon.⁸⁰ With this, CFD approximations or surrogate modeling would suit as better options to modeling the potential occurrence of balling, however are not integrated in this approach for previously mentioned reasons.

2.3 Model Context Protocol

The Model Context Protocol (MCP) is a standard introduced by Anthropic⁸¹ which provides guidelines for used functionality such as tool calling and resource querying; Particularly suitable for agentic tasks.^{47,82-84} Along with these features, MCP is compatible with the wider ecosystem of LLM providers with integrations in Software Development Kits (SDKs) developed by Anthropic,⁸² OpenAI,⁸⁵ Google,⁸⁶ and others.⁸⁴

2.3.1 Tools

Tools are the primary means in which an LLM is able to perform actions via MCP, invoking external Application Programming Interfaces (APIs) or function calls with the user's approval.⁸²⁻⁸⁴ Complexity of these tool calls can range from simple stateless actions (network requests to external APIs) or long-lived function operations (simulation runs).⁸² Using the MCP Python SDK,⁸² these tools can be exposed to the LLM with the appropriate decorator function configuration as seen in Appendix A. A minimal configuration consisting of the decorator wrapping a tool function is sufficient to register a tool for an LLM. However, additional annotations such as type declarations, docstring descriptions, and structured outputs significantly improve the model's comprehension and proper utilization of the defined tool.

2.3.2 Resources

Resources provide the LLM capability to search for relevant information regarding a given task. Similar to GET requests established within the Hypertext Transfer Protocol (HTTP),⁸² this allows for the query of information stored within databases, filesystems, or other means to be accessible to the LLM.^{83,84} This is particularly useful during the tool calling process as it provides environmental state information regarding around the model. However, during experiments the LLM’s utilization of the resource functionality proved unreliable and tools implementing the same functionality of each resource displayed consistently reliable responses.

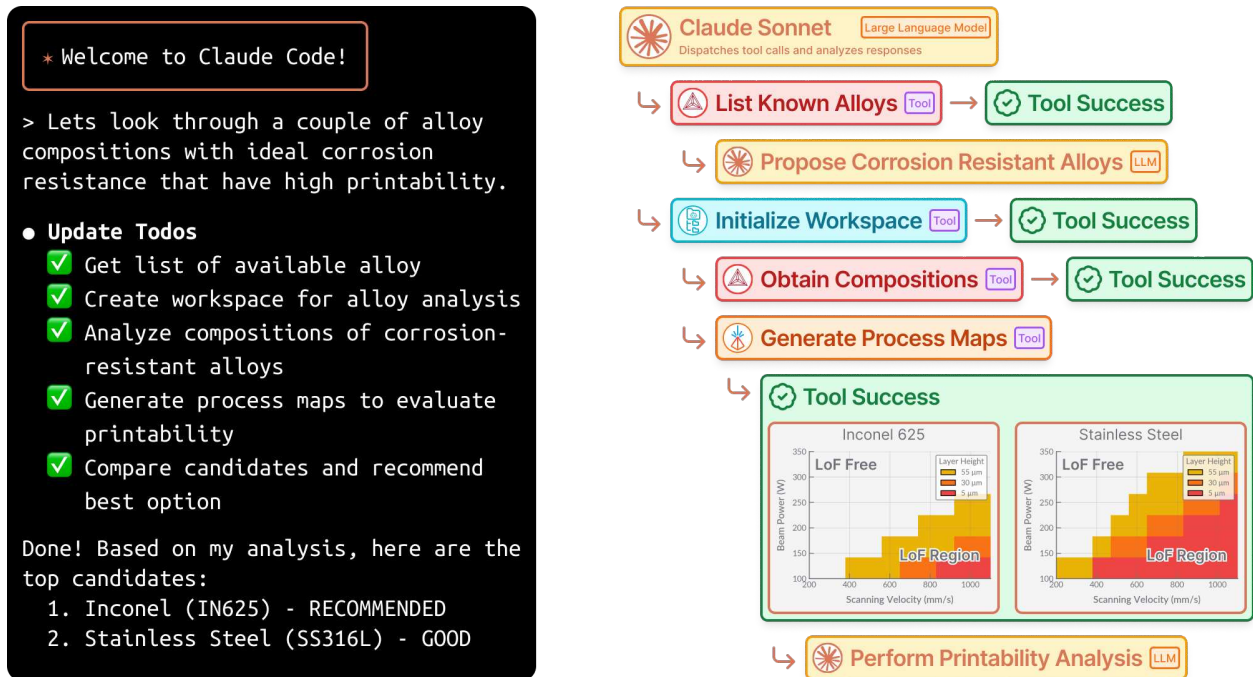


Figure 2: **(Left)** Claude Code provides an interface for integrating agentic tools with Claude Sonnet LLM, allowing for natural language input to execute tasks and response analysis. **(Right)** Streamlined summary of tool executions and analysis from the prompt given to Claude Code utilizing subagents for Additive Manufacturing, Thermo-Calc, and Workspace.

2.4 Agentic Tools

Tools developed for this application are separated into three different MCP Servers with Python Package Index (PyPi)⁸⁷ identifiers: `additive-manufacturing`, `thermo-calc`, and `workspace-agent`. Each of these packages maintain their own MCP server tools and *Sub-agent*⁸⁸ (a simple markdown file providing additional context and system prompts to guide tool usage) and are capable of standalone usage. Claude Code⁸⁹ provides a platform for coupling these tools into a multi-agent environment utilizing Claude Sonnet 4⁹⁰ as the primary large language model for orchestrating tool calls and performing response analysis.

2.4.1 Workspace

The `workspace-agent` package, abbreviated to `wa` internally, is responsible for the initialization and management of workspaces within the context of tool calls. It primarily acts as a state management tool for storing JSON serialized class objects and deserializing the stored JSON files to use within tools. This approach allows for different tools to use the same Python class methods and state since the input types to each tool are limited to primitives accessible via command line. Thus, filename references to serialized JSON files are provided as inputs to be loaded and deserialized within each tool since string, int, and formatted list and dict types are valid inputs to tools but Python instances of classes or functions are not.

Workspaces can be initialized via tool call (Figure 3) and are subdivided into top-level subfolders (i.e. `compositions`, `materials`, `process_maps`, etc.) containing state and responses for a given domain. Tools to list existing subfolders and their contents act as guides to help the LLM navigate through potential tool input arguments narrow the search window to the most applicable candidates. In addition to being listed as tools, functionality to list subfolders and their content are also exposed as resources accessible via MCP allowing for the LLM and user interface to obtain this information implicitly via syntax (i.e. `@workspace://{workspace}/{subfolder}/`).

The MCP server for workspaces operates independently, acting without direct knowledge

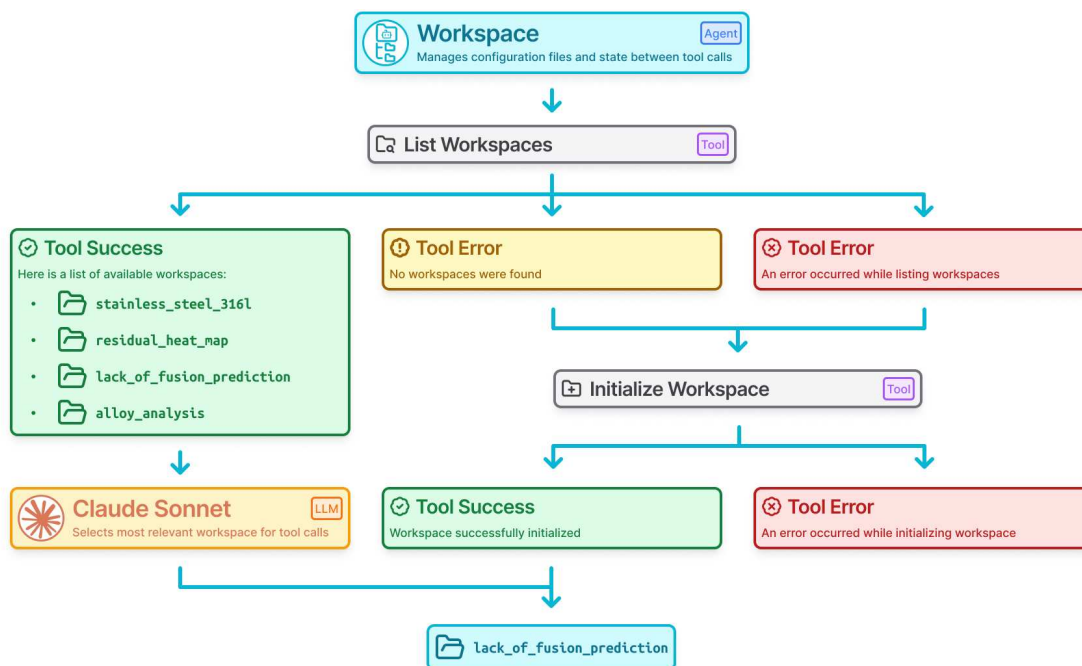


Figure 3: A simple tool calling procedure within the Workspace subagent for the task of finding or initializing a workspace. Here an initial tool call is made to list available workspaces and if none are found, a new workspace is created. This newly initialized workspace or the most relevant selected by Claude Sonnet is included in the successful response object.

of other installed MCP servers relying only on the LLM context to provide the appropriate arguments for workspace names and subfolders to navigate. This architecture allows for the other MCP servers to utilize workspace functionality preventing the issue of tool overlap between packages. This opinionated approach allows for MCP servers that utilize `workspace-agent` to share workspace subfolders such that the output of one MCP server’s tool can be utilized as an input to another MCP server tool.

2.4.2 Thermo-Calc

For this project, the authors developed and published a package with the PyPI⁸⁷ identifier `thermo-calc` (aliased internally as `tc`) to facilitate the installation and use of Thermo-Calc’s TC Python module.⁴⁸ Along with these installation scripts, Command Line Interface (CLI) and MCP bindings were also implemented for a subset of TC Python’s functionality, those of which are outlined in Section 2.1. With the set of tools managed by the `thermo-calc`

subagent, the material properties of a given alloy composition can be calculated and saved to a shared material configuration that the tools from `additive-manufacturing` can then utilize for process map generation.

In this process, an hypothetical alloy composition element or an existing element name is provided to the large language model in order to create an alloy composition file (Figure 4). An alloy composition file is produced by serializing provided element proportions to a JSON file consisting of element keys and mass fractions. (i.e. `{"Fe": 0.9, "C": 0.1}`) Both approaches eventually utilize the alloy composition schema tool, however if the subagent is provided a generic alloy name, it utilizes tools to list known alloys and obtain their compositions to then pass into the alloy composition schema tool.

Once the alloy composition is obtained, the TC-Python API is called to instantiate a server to calculate the Property Diagram for the given set of elemental compositions and temperature range. This returns a `PropertyDiagramResult` which is then saved for later use when calculating phase transition temperatures and other material properties. In a separate tool call, the `PropertyDiagramResult` is loaded for the volume fraction calculation of the liquid phase which the liquidus and solidus phase transition temperatures can be extracted from. The liquidus, solidus, and melting (midpoint between liquidus and solidus) are then saved into a phase transitions temperatures configuration file and utilized later in the calculation of other material properties and serialization of the material schema.

The previously calculated values are managed by `workspace-agent` package and are saved in the `property_diagrams`, `phase_transition_temperatures`, and `compositions` subfolders respectively. The relevant configurations are loaded from these subfolders into the material compilation tool which determines the values for the remaining material properties, those being specific heat capacity, density, thermal conductivity, and absorptivity. These values are instantiated as `Material` class and serialized into the `materials` subfolder as a JSON file for lack of fusion process map generation.

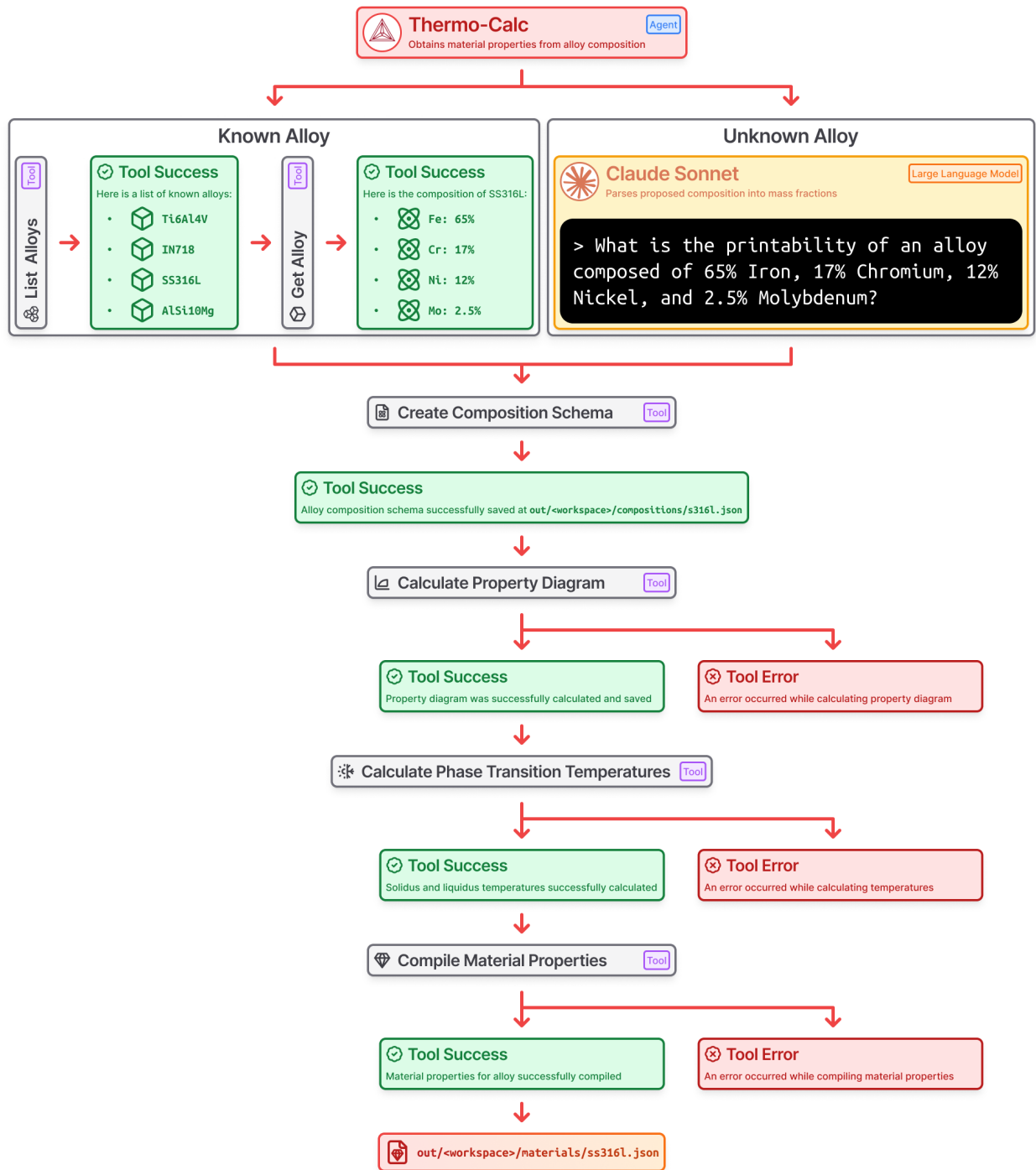


Figure 4: Flow diagram outlines the expected tool calling procedure for the Thermo-Calc subagent. In this example the material properties for Stainless Steel are extracted from the calculated property diagram of the alloy’s elemental composition. Composition is obtained from a look-up table of known alloys or provided directly to the agentic system and parsed into mass fractions using Claude Sonnet. This process generates a schema file with alloy’s material properties recorded for downstream use with other tools.

2.4.3 Additive Manufacturing

The `additive-manufacturing` (`am`) package provides a set of tools to assist with the additive manufacturing build process, currently built around providing feed forward solutions to predict potential build defects and gauge its feasibility. Of the available features, the experimental setup primarily utilizes the package's process map generation capabilities in order to predict potential lack of fusion defect regimes. The exact process for computing the melt pool dimensions necessary for determining the lack of fusion defect regime is outlined in Section 2.2, but in short, melt pool dimensions are calculated using an equation from Rosenthal³⁰ and fed into the lack of fusion defect criterion (Equation 3) to classify the input process parameter combination. In the current implementation classifications are limited to within or outside the lack of fusion defect regime as the analytic solution only works for conduction mode and cannot model melt pools in keyhole mode.³⁰

Process map generation is managed by the additive manufacturing subagent responsible for the relevant tools within its MCP server (Figure 5). To achieve this configuration files for desired materials and build parameters need to be created before the process map can be initialized and generated. Material configuration contains material dependent properties such as density, thermal diffusivity, thermal conductivity, and liquidus and solidus phase transition temperatures to name a few. Build configuration manages values such as beam power, scan velocity, layer height, and hatch spacing. These configuration files are utilized by the process map initialization tool which creates the subfolder for storing process map results and the process map configuration file for overriding build parameter configurations of beam power and scan velocity. Instead of a single scalar value, process map configuration file overrides the build configuration file with a range of values as to use the same material and build configurations when calculating defect regimes but with either a different power or velocity. The default process map range for power and velocity is 100 to 1000 with steps every 100 W or mm/s respectively. With this, the necessary calculations are performed to obtain lack of fusion regimes for 2 layer heights ($-25 \mu m$ and $+25 \mu m$) in addition to the

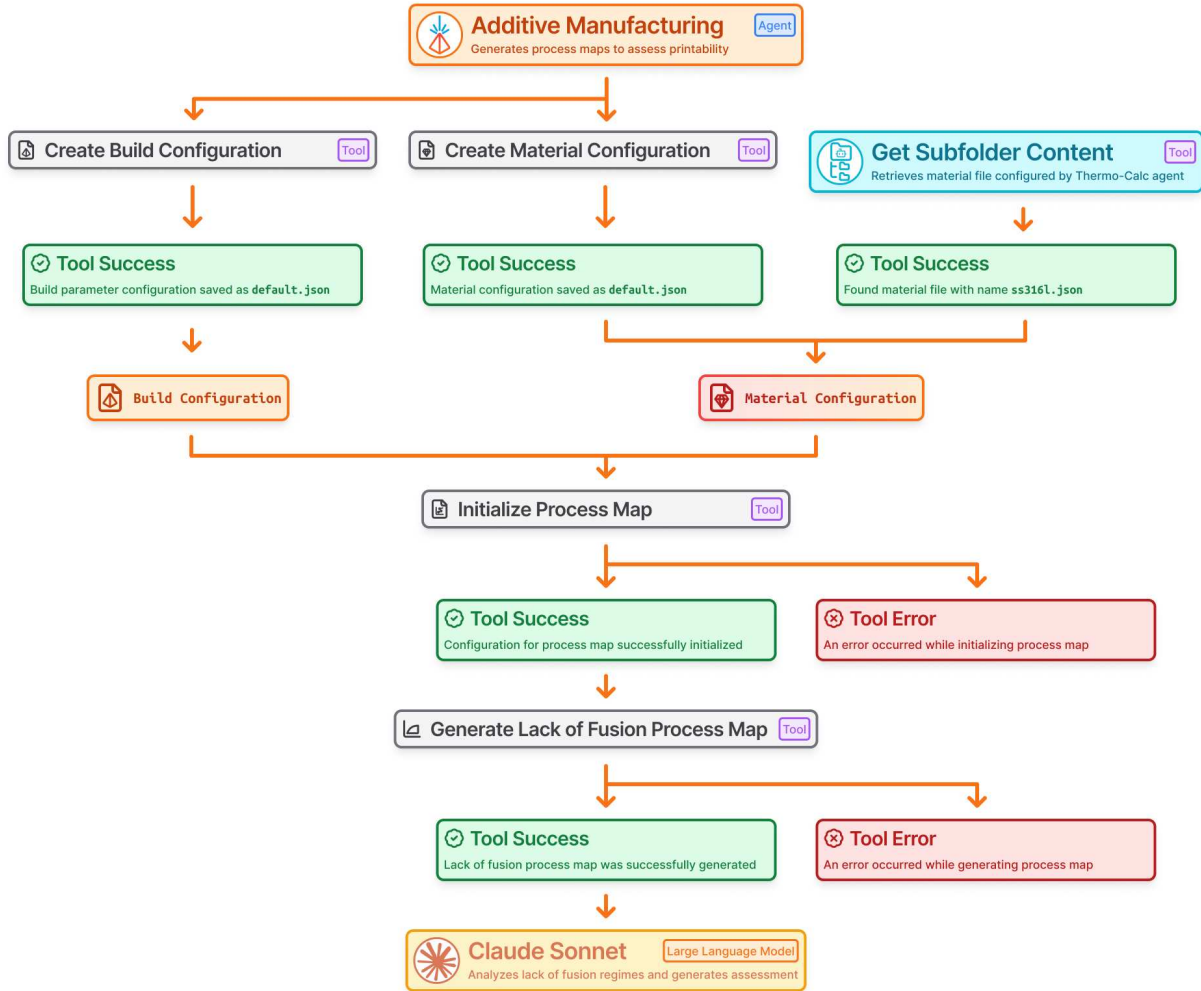


Figure 5: Diagram outlines expected tool calling procedure for additive manufacturing sub-agent for the task for generating and analyzing a lack of fusion process map. Build and material configurations are required to initialize a process map, the latter of which can be obtained from the Thermo-Calc subagent or manually configured by the additive manufacturing subagent. Initializing the process map provides override ranges for power and velocity build parameters for melt pool depth calculations. The tool generates the process map and a response consisting of power and velocity configurations that potentially exhibit lack of fusion defects. Claude Sonnet analyzes this response and provides suggestion for optimal build parameters.

prescribed layer height within the provided range of process parameters.

The Command Line Interface (CLI) provides the basic means of interaction with the `additive-manufacturing` package, however with its MCP integration, inputs and arguments can be left unstructured and functionality is accessible through just natural language when utilized as tools within an MCP server. In addition to natural language functionality, its integration with an LLM (i.e. Claude Sonnet) augments the capabilities of the user enabling easy evaluation of follow-up changes and LLM enabled analysis and feedback of computed results. Through the `workspace-agent` package, material configurations generated with the `thermo-calc` package can be utilized for the generation of process maps, allowing for the end-to-end functionality of proposing alloy compositions to analyzing their lack of fusion process map.

2.5 Experiments

Several experiments were performed to investigate the capability of the agentic system. Each experiment consists of a simple prompt regarding the desired alloy or material properties to explore (as shown in Figure 2) with the expected generation of a lack of fusion process map along with analysis and suggestion of potential printing parameters to implement. The whole of these experiments aims to cover the wide range of potential use case scenarios supported with the provided tools ranging from known and novel alloy compositions to searching and assessing alloys with a desired material property characteristic.

2.5.1 Known Alloy Compositions

Within the scope of known alloys, the system is expected to adhere to the established approach to obtaining a process map for a given material compositions with the caveat of obtaining these alloy composition from a provided dictionary. In this task it is expected that the LLM only acts to dispatch tools and interpret their subsequent response. This approach would be evaluated on a subset of the known alloys which include: Stainless Steel

316L, Titanium, Inconel, Aluminum, Tool Steel, Iron, Copper, Hastelloy X, K500, Tungsten, Bronze, and Aluminum 7050.

2.5.2 Material Property Search

For an open ended task, such as that encountered during the search for an alloy composition with specific desirable material properties, the large language model is utilized more. In this case, a similar approach to that of the known alloys is taken to determine an alloy's lack of fusion regime with an initial query given to the LLM to provide a list of candidates with the desired material properties. This included properties such as corrosion resistance, fatigue life, yield stress, Young's modulus, fracture toughness, hardness, and ductility.

2.5.3 Novel Alloy Compositions

The LLM is able to interpret a combination of elements into their respective mass fractions and call the relevant tools to determine the alloy's lack of fusion regime. Compositions outside that of the known alloys were also included in this investigation which primarily entailed the modification of existing alloy compositions such that an element was to be removed or the proportion of one was to be increased. In addition, the agentic system also accepts an hypothetical combination of elements along with their prescribed proportions. This hypothetical combination of elements provides the freedom to combine various elements, such as 50% Fe and 50% N, into the system but in practice is limited by the bounds of thermodynamic calculations and databases of Thermo-Calc. The system was primarily evaluated with compositions ranging from slight modifications of known alloys with a couple of completely hypothetical combination of elements to element compositions proposed by the LLM.

3 Results

For the known alloys, the lack of fusion process map was obtained using the provided alloy composition. In these experiments, the large language model is responsible for the selection of build parameters along with defining the appropriate process map range within the power and velocity process parameters. Of the 12 alloys this experiment was performed upon, 11 were able to produce a suitable lack of fusion process map (Figure 6). The one failure in this case occurred with the Tool Steel prompt which resulted in the process hanging while utilizing the property diagram calculation tool. This is potentially due to the number of potential options for "Tool Steel" that the MCP tool had available such as "D2 Tool Steel", "M2 Tool Steel", "A2 Tool Steel" which required further clarification.

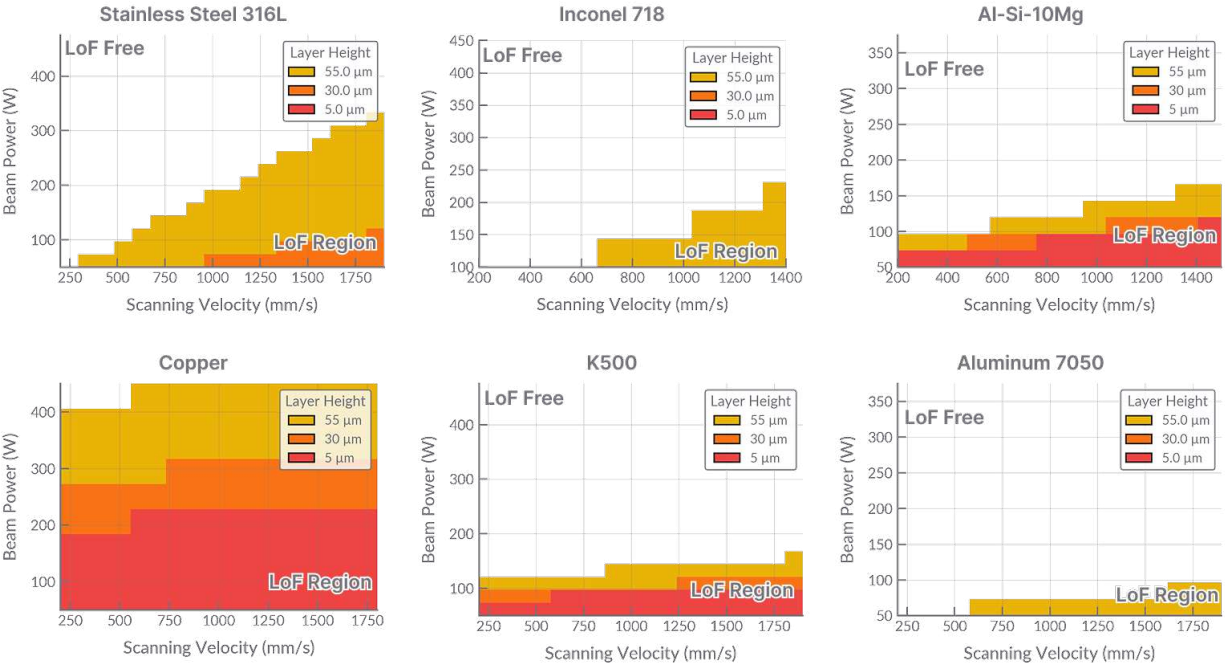


Figure 6: Lack of fusion process maps for a selection of known alloys with default hatch spacings of $50\mu\text{m}$ and various layer heights indicated by their respective colors within the legend.

When prompted to search for an alloy with a specific material property, the LLM reasons through number of potential candidates and selects a couple to evaluate. The same procedure is taken for generating process maps for each alloy candidate the results of which

are evaluated and compared with emphasis towards minimizing lack of fusion (Figure 7). Of the 9 investigated material properties, the agentic system failed to produce process maps for only one of the cases. The failure case occurred while comparing creep resistance of various alloys, specifically when attempting to generate the process map investigating the nickel based superalloy, Mar-M 247. Besides this exception, all prompts were successful in creating lack of fusion process maps and performing analysis and recommendations based on the feasibility of each alloy candidate.

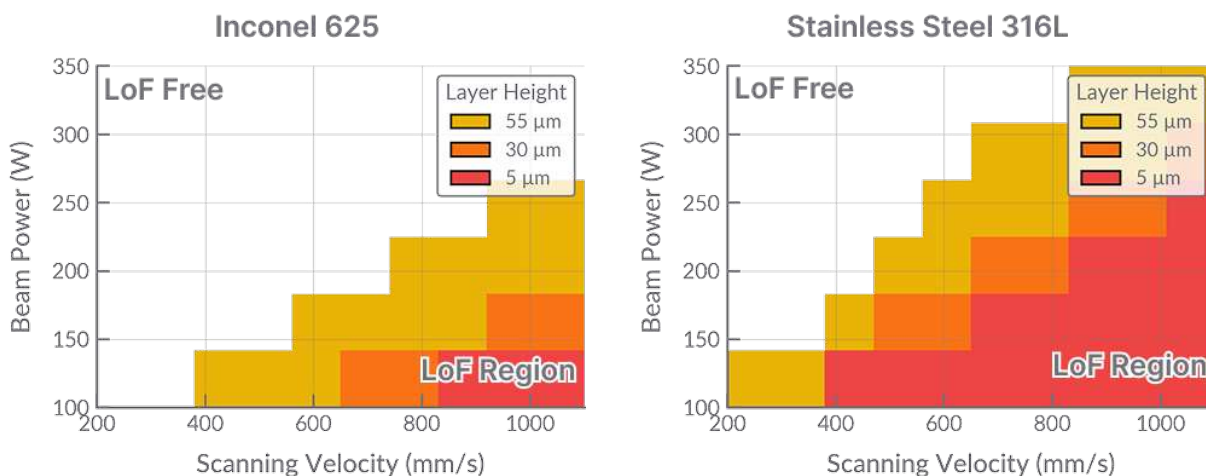


Figure 7: Comparison of lack of fusion process maps of between Inconel 625 and Stainless Steel 316L for corrosion resistant applications. Between these two candidates, the LLM ultimately recommended the use of Inconel 625 for its smaller lack of fusion regime.

For the application of corrosion resistance (exact prompt and response provided in Appendix F), the additive manufacturing subagent recommendation of Inconel 625 aligns with the findings from multiple literature sources.⁹¹⁻⁹³ In a study by Zhang et al.,⁹¹ the authors investigate corrosion resistance of Inconel 625 and Stainless Steel 316L hybrid alloys under the application of hydrofluoric acid. Inconel is stated to have greater corrosion resistant properties than that of Stainless Steel 316L however, due to its higher Nickel and Chromium content the manufacturing cost is higher as well.⁹¹ Process parameter combinations used with Inconel 625 range from 175 W and 500 mm/s⁹⁴ to 1000 W and 600 mm/s,⁹¹ all of which are valid process parameters within the prediction of the additive manufacturing subagent.

For novel alloys, compositions are directly evaluated and in some instances produce rather extreme process maps. Of the 10 conducted experiments, 8 were successfully able to produce process maps with 2 failing due to the nature of the alloy composition. Although the system accepts any composition of elements, most hypothetical combination of elements are unsuitable for printing and practical use. As such, slightly adjusting known alloy combinations produces more suitable lack of fusion regimes as seen in the cases where Molybdenum is removed for Stainless Steel 316L or Inconel 625 (Figure 8).

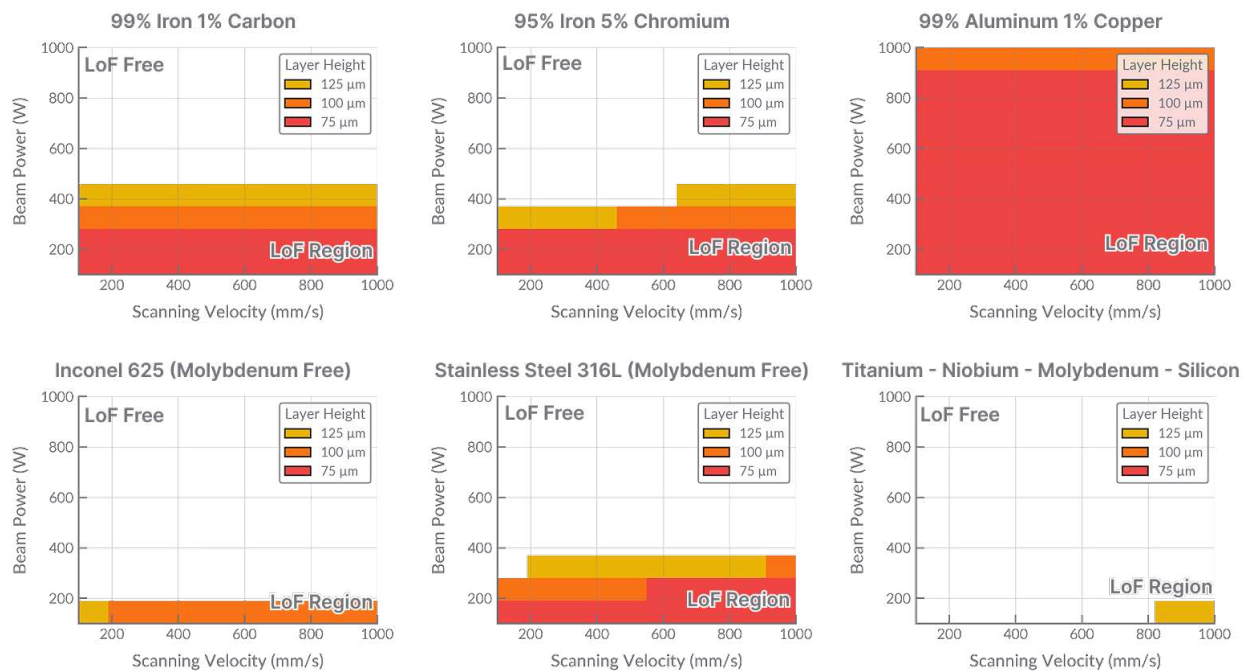


Figure 8: Various lack of fusion process maps for novel alloy compositions. **(Top Row)** Hypothetical element compositions for proposed Iron and Aluminum based alloys. **(Bottom Row)** slightly modified known alloy compositions of Inconel and Stainless Steel 316L with the removal of Molybdenum. **(Bottom Right)** An LLM proposed composition when prompted to suggest an novel alloy.

3.1 Lack of Fusion Validation of Known Alloy Compositions

Validation was performed on a couple of the common predicted alloy compositions (IN718 and SS316L) to ensure the predicted lack of fusion process aligned with what is found within the literature. In addition, the expected material properties associated with each alloy along

with the associated processing parameters were included to provide broader context to what is expected from each alloy.

3.1.1 Inconel 718

Validation of the lack of fusion predictions of known alloys indicate satisfactory overlap between those generated by additive manufacturing subagent and that found within published literature. In a study by Ghanadi et al.,¹⁴ lack of fusion was observed at laser powers between 50 to 150 Watts and scan speeds of 700 mm/s to 1200 mm/s when conducted with a prescribed layer height of $25\mu\text{m}$ and hatch space of $40\mu\text{m}$. These process parameters are similar to those implemented using the additive manufacturing subagent ($50\mu\text{m}$ hatch spacing and $30\mu\text{m}$). Although the generated process map for Inconel 718 (Figure 6) denotes a slight under prediction of lack of fusion compare to that of the literature, this can be attributed the more general applicability of Rosenthal's equation.³⁰

The study provides areal surface roughness (Sa) of the top and sides of their printed lattice structure as an indicator for lack of fusion. The authors observed the expected trend that the Sa values decreased with increasing laser power and increasing scan speed, where the lowest Sa value of $26.5 \pm 5.4 \mu\text{m}$ with an ultimate shear strength of $153.2 \pm 7.7 \text{ Mpa}$ and shear strain of 0.33 ± 0.02 at 150 Watts and 200 mm/s.¹⁴ The highest Sa occurrence of $70 \pm 8.9\mu\text{m}$ with an ultimate shear strength $8.93 \pm 0.9 \text{ Mpa}$ and 0.69 ± 0.03 shear strain recorded at a 50 Watts and 1200 mm/s power and velocity combination.¹⁴

3.1.2 Stainless Steel 316L

The generated process map for Stainless Steel 316L (SS316L) matches the lack of fusion regimes outlined in the literature, with unfavorable process windows at lower powers and higher velocity combinations.^{20,95,96} Ahmed et al.⁹⁵ encounters high densification of SS316L at power and velocity combinations of (150 W, 500 mm/s), (200 W, 700 mm/s), (250 W, 900 mm/s), and (300 W, 1100 mm/s), matching that presented in Figure 6.

Within the lack of fusion defect regime, the resulting pore size is heavily dependent on the factors of height and width of the melt pool along with the hatch spacing and layer height of the build.^{97,98} For hatch spacings ranging from 25 μm to 55 μm , equivalent pore sizes upwards of 160 μm can be observed (power at around 100 W, 30 μm layer height, and 1.4 m/s scan velocity).⁹⁸ Within the range of scan velocities from around 1.05 m/s to 1.75 m/s, an average pore diameter of around 30 μm with a standard deviation of 16 μm and approximate maximum of 130 μm was observed (with previously mentioned process parameters and 50 μm hatch spacing).⁹⁸

In more nominal processing conditions, the percentage of porosity within a part is observed to change as a function of energy density. This is reflected in work by Tucho et al. where the authors manufactured a number of samples and recorded that porosity by volume within a part decreases from over 3% with energy densities of around 50 J/mm³ to less than 1% at energy densities of 65 J/mm³.⁹⁹ The authors also found that hardness increases linearly with energy density as a hardness values of 188 ± 4 HV was observed at an energy density of 80 J/mm³ from a value of 168 ± 15 HV at an energy density of 50 J/mm³.⁹⁹ With regard to mechanical properties, it was found that tensile strength and yield strength could be improved through layer remelting as Lu et al. recorded a respective increase from 674 MPa to 725 MPa and 591 MPa to 643 MPa with process parameters of power at 250 W, scan velocity at 950 mm/s, hatch spacing of 110 μm , and layer height of 30 μm .^{95,100}

4 Discussion

In this agentic system, all tasks are completed with tools performing deterministic actions; the large language model merely orchestrates and analyses the response of dispatched tool calls. As a result, fidelity of the system's predictions relies primarily on the accuracy of the developed tools. To that point, this work limits its process map prediction to the lack of fusion regime as it utilizes a conduction mode limited analytical approach to obtain melt

pool dimensions.³⁰ With these separation of concerns, determining the source of invalid predictions is simplified where incorrect evaluation of results can be attributed to the large language model and production of inaccurate predictions can be assigned to the tool.

Within the experimental trials a few prompts produced incorrect results as such was the case in evaluating a material with optimal hardness. In this case the lack of fusion process maps were correctly generated however the LLM recommended the use of Enhanced Maraging Steel over the other two candidates (Figure 9). From visually interpreting the process maps, it is clear that Enhanced Maraging Steel has the largest lack of fusion regime when compared to its counterparts. One potential cause of this misinterpretation could be attributed to the response data structure returned to the LLM after a tool call. Since the lack of fusion regimes are returned as power and velocity combinations within a list of tuples (i.e. $[(100, 100), (150, 100), \dots]$), the LLM may have misinterpreted these values to be valid process windows rather than lack of fusion regimes. Proper key names and serializing of results would help reduce these types of LLM mistakes.

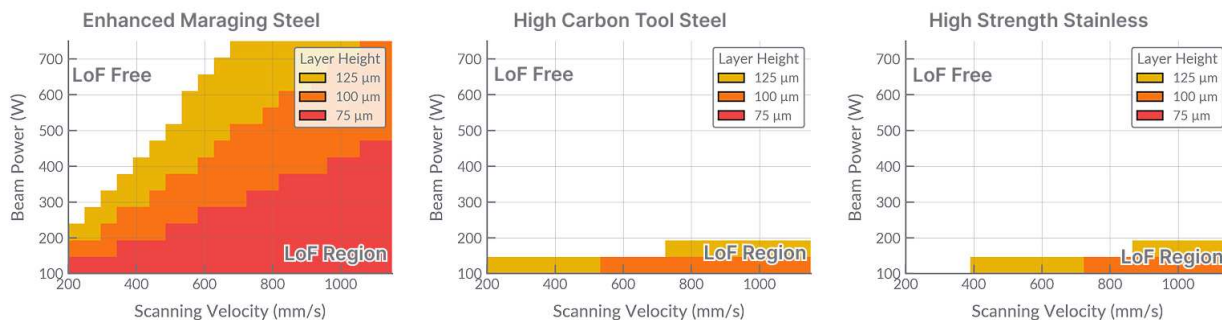


Figure 9: High hardness alloy candidates with their respective lack of fusion process maps. LLM makes an error by recommending Enhanced Maraging Steel over High Strength Stainless Steel for its smaller lack of fusion region.

The deterministic nature of these tools does present the question of the benefit of introducing an LLM into the system, as if the tools can work on their own individually, what would be the purpose of including an LLM into the architecture. This is a valid concern as the common workflows of each tool can be connected to each other through a parent script, achieving the same effect. However, the inclusion of an LLM and the separation of

tools into their own subagents allows for several unique capabilities. The most apparent of these is the utilization of natural language when interacting with the developed tools. This allows the user to directly interact with the available tooling without explicitly adhering to the strict syntax and argument guidelines required by the CLI. Another is the LLM’s ability to analyze results providing user interpretive feedback on a tool’s response. This supports another key ability of LLM agents which is to establish a feedback loop and respond to changes within its context. The integration of LLM Agents within the developed tools not only enhances the user experience with these tools but establishes an automation framework enabling researcher to efficiently utilize their available tools.

4.1 Comparison to Existing Tool Integration Frameworks

Other alternatives to tool calling and agentic system frameworks exist to the Model Context Protocol (MCP) such as LangChain⁴⁵ and LlamaIndex,⁴⁶ however, these approaches lack first party integration into the LLM that MCP provides. The alternative approaches are no less capable than MCP and have their own specific features as seen in other various agentic works.^{37,101} The primary reasoning behind using MCP as the framework for designing the agentic tools is expected long term support and ease of use that the protocol provides when applied to other models and the broader support it has with providers such as Anthropic, Google, and OpenAI. Although much of these tests were performed with the Claude model from Anthropic, initial implementations show that these experiments can be performed on the latest models from OpenAI (ChatGPT) and Google (Gemini) as well.

5 Conclusion

This multi-agent system augments the researcher’s ability to investigate and evaluate known and novel alloy compositions for processing via additive manufacturing. This is achieved through invoking tool calls via the Model Context Protocol (MCP) to perform thermo-

physical calculations and melt pool dimensional approximations to generate a lack of fusion process map. In addition, these tools can leverage the generalized knowledge of LLMs to assist in more generalized tasks such as suggesting alloy compositions for desired material properties through querying its large base of knowledge. The predictions from this system provide a suitable starting point of process parameters for experimental trials that would avoid potential areas of lack of fusion. Expansions upon this work would explore a more comprehensive search for processing parameters that would also consider the keyholing and balling defect regimes. This work sets the foundation for complex tool usage and automated research within the additive manufacturing field.

6 Future Work

Although the authors have provided a comprehensive study on the use of agentic tools within the additive manufacturing space, there remain a couple of aspects to this work that would benefit from further research.

6.1 Technical Roadmap

6.1.1 Objective

Extension upon this work would expand upon the generation of a robust process map which considers additional build parameter and processing factors such as beam size, melt pool fluid dynamics, and varying absorptivity. Specifically, process regimes for keyholing and balling would be incorporated into the final alloy evaluation when selecting a set of build parameters within a process window. Additionally, validation of novel alloy compositions and process parameters proposed by the agentic system would include fabricating samples evaluation through tensile tests.

6.1.2 Methodology

In order to obtain melt pool dimensions which more accurately match those created experimentally, a more comprehensive solver will need to be utilized. Options include CFD solvers developed by FLOW-3D,³² OpenFOAM,³¹ or one specifically for the purpose of defining defect regimes. With each of these approaches, the tradeoff between computational cost and accuracy would be of primary concern.

Within the agentic system, the overall framework will still build upon the Model Context Protocol and further utilize features such as resources and tool calling. Design improvements would include tool consolidate to reduce potential tool bloat and clarify adjustments to reduce the frequency of faulty tool calls. Additionally, consideration towards optimizing token and time cost between various LLM providers will be incorporated as well.

6.1.3 Evaluation Metrics

Evaluation of the updated solver will compare the melt pool dimensional values to those observed within the literature. Metrics here will include the percent error observed between the two dimensional measurements. Additionally, the solver's ability to model behaviors such as balling and keyholing will be scrutinized further and the computed defect regimes will be contrasted to those found within the literature.

Sample fabrication would have a more qualitative evaluation metric as machine or composition specific factors may hinder the manufacturing of parts consisting of novel alloy compositions. A scenario where the novel composition sample is ultimately fabricated but under a certain process conditions not mentioned by the agentic system. After fabrication, the mechanical properties such as yield strength, ultimate tensile strength, and hardness would be evaluated as well.

6.1.4 Timeline

The objectives outlined within this technical roadmap such as improvements to the agentic system are currently in progress and will be expanded upon further in a future work. Other considerations such as part fabrication and mechanical testing relies on the selection or development of a CFD solver that can produce more accurate melt pool dimensions suitable for a more comprehensive process map.

7 Data Availability

The multi-agent system developed for this work along with the data associated with experimental prompts are available at the following link: <https://github.com/BaratiLab/Agentic-Additive-Manufacturing-Alloy-Evaluation>. The various tools within the agentic system are hosted on the Python Package Index (PyPI) and installable with their respective package names: `additive-manufacturing`, `thermo-calc`, `workspace-agent`.

Appendix A Model Context Protocol Example Tool

```
1 @app.tool(  
2     title="Run Layer with Solver",  
3     description="Runs solver on a segments file (segments file  
4         should be one layer) and saves the generated meshes.",  
5     structured_output=True,  
6 )  
7 def solver_run_layer(  
8     workspace: str,  
9     segments_foldername: str,  
10    layer_number: int,  
11    build_config_filename: str = "default.json",  
12    material_config_filename: str = "default.json",  
13    mesh_config_filename: str = "default.json",  
14    run_name: str | None = None,  
15 ) -> Union[ToolSuccess[Path], ToolError]:  
16     """  
17     Runs solver for segments at a specified layer number.  
18     Args:  
19         workspace: Folder name of existing workspace  
20         segments_foldername: Folder name of where segments are  
21             expected to be found.  
22         layer_number: Layer number to run solver on, typically  
23             starts from 1. For testing out, try skipping the first  
24             several layers as those sometimes don't include part  
25             geometry.  
26         distance_xy_max: Maximum segment length when parsing (  
27             defaults to 1.0 mm).  
28         build_config_filename: build config file to use with solver.  
29         material_config_filename: material config file to use with  
30             solver.  
31         mesh_config_filename: mesh config file to use with solver.  
32         run_name: Name of folder to save generated meshes at,  
33             typically autogenerated.  
34     """  
35     ...
```

Figure 10: Example tool implementation shown via Solver tool defined in additive-manufacturing package.

Appendix B Melt Pool Length

Rosenthal's equation³⁰ can be rewritten to provide the bounds for the melt pool. If z is substituted with R , the width of the melt pool shrinks to zero and becomes the furthest point in the melt pool.

$$z = R + \frac{2\alpha}{V} \ln \left(\frac{2\pi k R \Delta T}{\epsilon P} \right) \quad (8)$$

$$R = R + \frac{2\alpha}{V} \ln \left(\frac{2\pi k R \Delta T}{\epsilon P} \right) \quad (9)$$

$$0 = \frac{2\alpha}{V} \ln \left(\frac{2\pi k R \Delta T}{\epsilon P} \right) \quad (10)$$

Since the coefficient term $\frac{2\alpha}{V}$ will be a non-zero value, ignore this term to simplify calculation.

$$\frac{2\alpha}{V} \neq 0; 0 = \ln \left(\frac{2\pi k R \Delta T}{\epsilon P} \right) \quad (11)$$

Taking the exponential of both sides and solving for R produces the following equation that provides the expected length of the melt pool from the heat source.

$$e^{\ln \left(\frac{2\pi k R \Delta T}{\epsilon P} \right)} = e^0 \quad (12)$$

$$\frac{2\pi k R \Delta T}{\epsilon P} = 1 \quad (13)$$

$$2\pi k R \Delta T = \epsilon P \quad (14)$$

$$R = \frac{\epsilon P}{2\pi k \Delta T} \quad (15)$$

Appendix C Database Selection

1. **Ti-based alloys:** if top element is "Ti" → TCTI6.
2. **Ni-based alloys:** if top element is "Ni" or the Ni fraction is ≥ 0.30 → TCNI12.
3. **Fe-based alloys:** if top element is "Fe" (and the previous Ni criteria were not satisfied) → TCFE14.
4. **Al-based alloys:** if top element is "Al" (and none of the above criteria applied) → TCAL9.
5. **Pure elements:** if we have a pure metal which is just a single element → PURE5.
6. **Fallback:** if none of the conditions above are met (maybe for MPEAs) → TCHEA7.

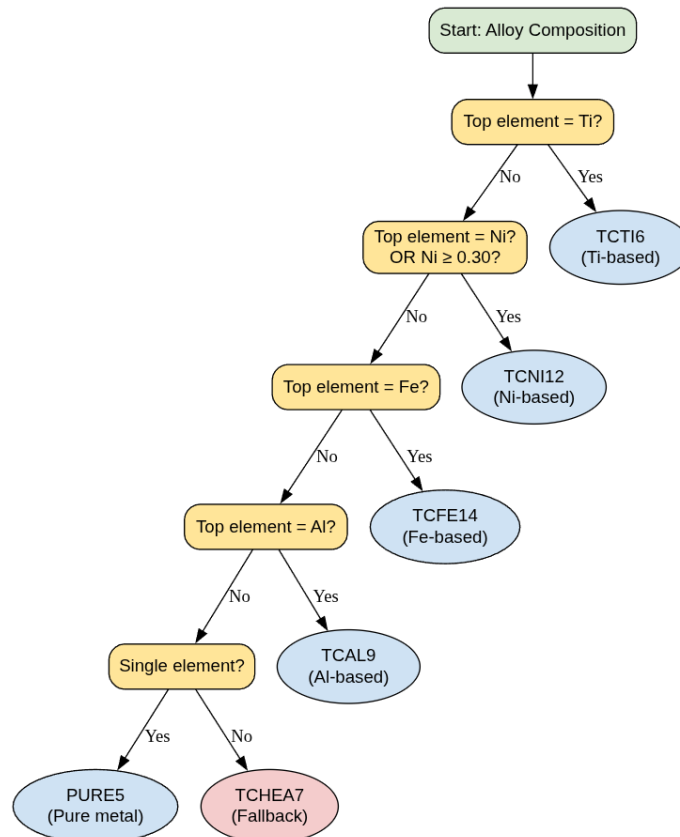


Figure 11: Database selection decision tree

Appendix D Validation of Predicted Absorptivity

Table 1: Comparison between reported (literature) absorptivity and Drude-model calculated absorptivity at 1070 nm.

Alloy	Reported Absorptivity	Drude-Model Absorptivity
SS316L	0.35-0.60	0.4479
Ti-6Al-4V	0.27-0.6	0.4520
Hastelloy X	0.45-0.64	0.4413
M300 Steel	0.35	0.43

Appendix E Lack of Fusion and Keyhole Boundaries of Known Alloys

Literature results for defect classifications regarding 316L Stainless Steel and Inconel 718 were analyzed to uncover potential lack of fusion and keyhole regions over a range of power and velocity combinations.^{76,102} Logistic Regression was applied to determine boundary between the keyholing and lack of fusion regions. With respect to SS316L, a higher degree of overlap between these two defect regimes is visible due to the greater amount of samples when compared to that of the IN718 plot (Figure 12).

The boundary set by logistic regression implies that given the two defection classifications, if a defect were to occur it would be either keyhole or lack of fusion since it is expected that between these two regions a nominal process window could exist. This boundary is utilized as a threshold to limit the extent in which the Rosenthal's equation can be applied to determine lack of fusion defects before exiting conduction mode. In addition, sensitivity analysis on the boundary was performed by removing data points with the keyhole classification and the boundary was calculated only with lack of fusion data points. This resulted in a more conservative boundary in which defects would be classified as lack of fusion.

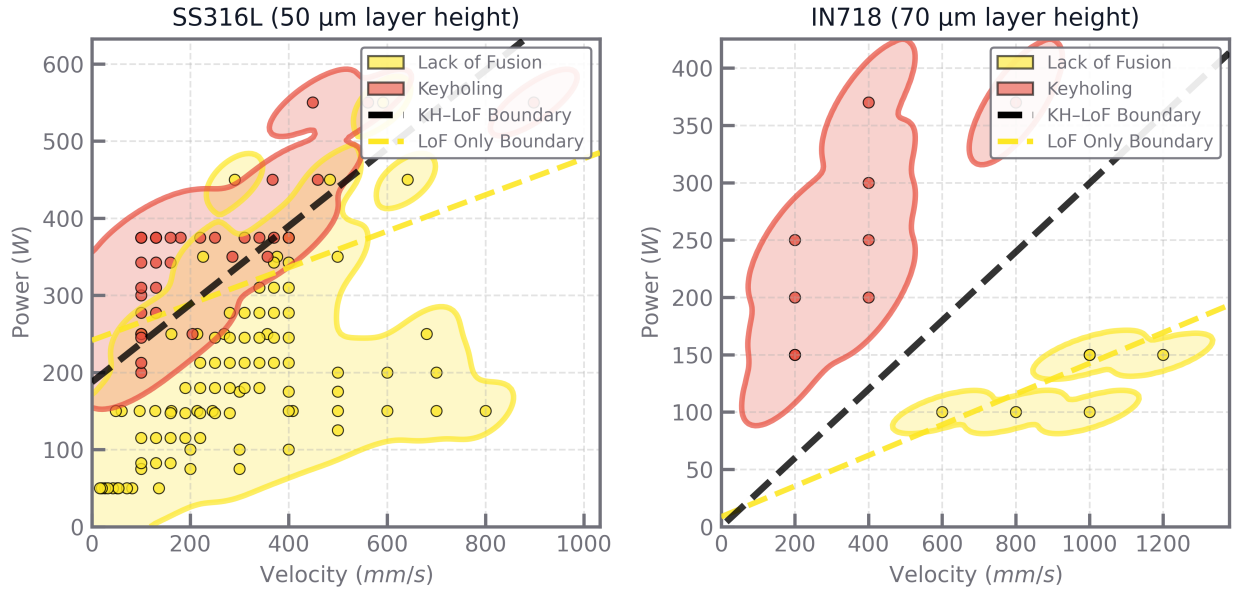


Figure 12: Literature values for SS316L and IN718 melt pool classifications expected defect regions for each respective alloy. Logistic regression is applied to establish a boundary between the two regions to reference as threshold to the extent in which Rosenthal's equation can be used to predict lack of fusion defects.

Appendix F LLM Prompt and Response for Corrosion Resistant Material Property Search

The following prompt was provided to the agentic system:

Lets look through a couple of alloy compositions to find a suitable candidate ideal for corrosion resistance that express high printability?

After successful tool calls, the LLM responded with the following:

References

- (1) Bandyopadhyay, A.; Heer, B. Additive manufacturing of multi-material structures. *Materials Science and Engineering: R: Reports* **2018**, *129*, 1–16.
- (2) Bandyopadhyay, A.; Traxel, K. D.; Lang, M.; Juhasz, M.; Eliaz, N.; Bose, S. Alloy

1 Based on my analysis of corrosion-resistant alloys, here are the top
 2 candidates:

3 IN625 (Inconel 625) - RECOMMENDED

4

5 Composition: 62.5% Ni, 22.9% Cr, 9.4% Mo, 5.2% Fe

6 - Corrosion Resistance: Excellent in marine, chemical, and high-
 7 temperature environments

8 - Printability: Superior - Only 3 lack-of-fusion conditions at low
 9 power (100W) with high velocities

10 - Process Window: Wide range of successful parameters (150-400W,
 11 200-1100 mm/s)

12 SS316L (Stainless Steel 316L) - GOOD ALTERNATIVE

13

14 Composition: 67.4% Fe, 17.6% Cr, 12.4% Ni, 2.6% Mo

15 - Corrosion Resistance: Very good, especially against chloride
 16 environments

17 - Printability: More challenging - 17 lack-of-fusion conditions at
 18 low power, 38 at higher layer heights

19 - Process Window: Narrower than IN625, requires careful parameter
 20 control

21

22 Key Findings:

23

1. IN625 shows superior printability with fewer defect-prone
 2 parameter combinations

3. SS316L has more extensive lack-of-fusion regions, particularly
 4 at 55 m layer height

5. Both alloys offer excellent corrosion resistance, but IN625
 6 provides better process reliability

7

8 Recommendation: IN625 is the optimal choice, combining exceptional
 9 corrosion resistance with superior additive manufacturing
 10 printability.

Figure 13: Prompt response and reasoning provided by agentic system for evaluating lack of fusion process map for known alloys.

design via additive manufacturing: Advantages, challenges, applications and perspectives. *Materials Today* **2022**, *52*, 207–224.

- (3) Ghafarollahi, A.; Buehler, M. J. AtomAgents: Alloy design and discovery through physics-aware multi-modal multi-agent artificial intelligence. 2024; <http://arxiv>.

org/abs/2407.10022, arXiv:2407.10022 [cs].

- (4) Tammam-Williams, S.; Todd, I. Design for additive manufacturing with site-specific properties in metals and alloys. *Scripta Materialia* **2017**, *135*, 105–110.
- (5) Polonsky, A. T.; Pollock, T. M. Closing the science gap in 3D metal printing. *Science* **2020**, *368*, 583–584, Publisher: American Association for the Advancement of Science.
- (6) Sames, W. J.; List, F. A.; Pannala, S.; Dehoff, R. R.; Babu, S. S. The metallurgy and processing science of metal additive manufacturing. *International Materials Reviews* **2016**, *61*, 315–360, Publisher: SAGE Publications.
- (7) Jadhav, Y.; Berthel, J.; Hu, C.; Panat, R.; Beuth, J.; Barati Farimani, A. StressD: 2D Stress estimation using denoising diffusion model. *Computer Methods in Applied Mechanics and Engineering* **2023**, *416*, 116343.
- (8) Rashid, A.; Gopaluni, A. A Review of Residual Stress and Deformation Modeling for Metal Additive Manufacturing Processes. *Chinese Journal of Mechanical Engineering: Additive Manufacturing Frontiers* **2023**, *2*, 100102.
- (9) Paul, R.; Anand, S.; Gerner, F. Effect of Thermal Deformation on Part Errors in Metal Powder Based Additive Manufacturing Processes. *Journal of Manufacturing Science and Engineering* **2014**, *136*.
- (10) Xu, Z.; Zhang, H.; Du, X.; He, Y.; Luo, H.; Song, G.; Mao, L.; Zhou, T.; Wang, L. Corrosion resistance enhancement of CoCrFeMnNi high-entropy alloy fabricated by additive manufacturing. *Corrosion Science* **2020**, *177*, 108954.
- (11) Pesode, P.; Barve, S. Additive manufacturing of metallic biomaterials and its biocompatibility. *Materials Today: Proceedings* **2022**,
- (12) Pesode, P.; Barve, S. Additive manufacturing of magnesium alloys and its biocompatibility. *Bioprinting* **2023**, *36*, e00318.

- (13) Jiao, C.; Xie, D.; He, Z.; Liang, H.; Shen, L.; Yang, Y.; Tian, Z.; Wu, G.; Wang, C. Additive manufacturing of Bio-inspired ceramic bone Scaffolds: Structural Design, mechanical properties and biocompatibility. *Materials & Design* **2022**, *217*, 110610.
- (14) Ghanadi, N.; Son, K.; Alvarado, M.; Yang, S.; Kao, H.-M.; Chang, C.-H.; Paul, B. K.; Pasebani, S. Effect of LPBF Processing Parameters on Inconel 718 Lattice Structures: Geometrical Characteristics, Surface Morphology, and Mechanical Properties. *Materials & Design* **2025**, *253*, 113864.
- (15) Edwards, P.; O’Conner, A.; Ramulu, M. Electron Beam Additive Manufacturing of Titanium Components: Properties and Performance. *Journal of Manufacturing Science and Engineering* **2013**, *135*.
- (16) Vrancken, B.; Thijs, L.; Kruth, J.-P.; Van Humbeeck, J. Heat treatment of Ti6Al4V produced by Selective Laser Melting: Microstructure and mechanical properties. *Journal of Alloys and Compounds* **2012**, *541*, 177–185.
- (17) Jelis, E.; Clemente, M.; Kerwien, S.; Ravindra, N. M.; Hespos, M. R. Metallurgical and Mechanical Evaluation of 4340 Steel Produced by Direct Metal Laser Sintering. *JOM* **2015**, *67*, 582–589.
- (18) Popovich, A.; Sufiiarov, V.; Polozov, I.; Borisov, E.; Masaylo, D.; Orlov, A. Microstructure and mechanical properties of additive manufactured copper alloy. *Materials Letters* **2016**, *179*, 38–41.
- (19) Lu, S. L.; Tang, H. P.; Ning, Y. P.; Liu, N.; StJohn, D. H.; Qian, M. Microstructure and Mechanical Properties of Long Ti-6Al-4V Rods Additively Manufactured by Selective Electron Beam Melting Out of a Deep Powder Bed and the Effect of Subsequent Hot Isostatic Pressing. *Metallurgical and Materials Transactions A* **2015**, *46*, 3824–3834.
- (20) Huang, G.; Chen, H.; Ma, Z.; Zhang, R.; Pei, J.; Lie, Z.; Du, P.; Peng, X.; Liu, Y.; Huang, K. Microstructure and mechanical properties of stainless steel additively man-

- ufactured via laser powder bed fusion in high-dense process parameter window. *Materials Science and Engineering: A* **2025**, *928*, 148033.
- (21) Martendal, C. P.; Esteves, P. D. B.; Lthi, C.; Deillon, L.; Afrasiabi, M.; Bambach, M. Mitigating defects at copper-steel interfaces via a lack of fusion-informed power increment strategy in multi-material laser powder bed fusion. *Materials & Design* **2025**, *258*, 114597.
- (22) Honarmandi, P.; Seede, R.; Xue, L.; Shoukr, D.; Morcos, P.; Zhang, B.; Zhang, C.; Elwany, A.; Karaman, I.; Arroyave, R. A rigorous test and improvement of the Eagar-Tsai model for melt pool characteristics in laser powder bed fusion additive manufacturing. *Additive Manufacturing* **2021**, *47*, 102300.
- (23) Tang, M.; Pistorius, P. C.; Beuth, J. L. Prediction of lack-of-fusion porosity for powder bed fusion. *Additive Manufacturing* **2017**, *14*, 39–48.
- (24) Tang, M.; Pistorius, P. C.; Narra, S.; Beuth, J. L. Rapid Solidification: Selective Laser Melting of AlSi10Mg. *JOM* **2016**, *68*, 960–966.
- (25) Tan, X.; Kok, Y.; Tan, Y. J.; Descoins, M.; Mangelinck, D.; Tor, S. B.; Leong, K. F.; Chua, C. K. Graded microstructure and mechanical properties of additive manufactured Ti6Al4V via electron beam melting. *Acta Materialia* **2015**, *97*, 1–16.
- (26) Kaufman, L.; Bernstein, H. *Computer Calculation of Phase Diagrams with Special Reference to Refractory Metals*; Academic Press, 1970.
- (27) Gheribi, A. E.; Chartrand, P. Application of the CALPHAD method to predict the thermal conductivity in dielectric and semiconductor crystals. *Calphad* **2012**, *39*, 70–79.
- (28) Campbell, C. E.; Kattner, U. R.; Liu, Z.-K. The development of phase-based property

- data using the CALPHAD method and infrastructure needs. *Integrating Materials and Manufacturing Innovation* **2014**, *3*, 158–180.
- (29) Eagar, T. W.; Tsai, N. S. Temperature fields produced by traveling distributed heat sources. *Weld. Res. Suppl.; (United States)* **1983**, Institution: Massachusetts Institute of Technology, Cambridge Number: CONF-830485-.
- (30) Rosenthal, D. The Theory of Moving Sources of Heat and Its Application to Metal Treatments. *Transactions of the American Society of Mechanical Engineers* **2022**, *68*, 849–865.
- (31) OpenFOAM. 2025; <https://www.openfoam.com/>.
- (32) FLOW-3D. <https://www.flow3d.com/>.
- (33) Zhang, Y.; Zhang, J. Modeling of solidification microstructure evolution in laser powder bed fusion fabricated 316L stainless steel using combined computational fluid dynamics and cellular automata. *Additive Manufacturing* **2019**, *28*, 750–765.
- (34) Strayer, S. T.; Templeton, W. J. F.; Dugast, F. X.; Narra, S. P.; To, A. C. Accelerating High-Fidelity Thermal Process Simulation of Laser Powder Bed Fusion via the Computational Fluid Dynamics Imposed Finite Element Method (CIFEM). *Additive Manufacturing Letters* **2022**, *3*, 100081.
- (35) Cunningham, R.; Nicolas, A.; Madsen, J.; Fodran, E.; Anagnostou, E.; Sangid, M. D.; Rollett, A. D. Analyzing the effects of powder and post-processing on porosity and properties of electron beam melted Ti-6Al-4V. *Materials Research Letters* **2017**, *5*, 516–525, Publisher: Taylor & Francis eprint: <https://doi.org/10.1080/21663831.2017.1340911>.
- (36) Cunningham, R. W. Defect Formation Mechanisms in Powder-Bed Metal Additive

Manufacturing. Ph.D., Carnegie Mellon University, United States – Pennsylvania, 2018; ISBN: 9780355952520.

- (37) Jadhav, Y.; Pak, P.; Farimani, A. B. LLM-3D print: Large language models to monitor and control 3D printing. *Additive Manufacturing* **2025**, 105027.
- (38) Ock, J.; Guntuboina, C.; Barati Farimani, A. Catalyst Energy Prediction with CatBERTa: Unveiling Feature Exploration Strategies through Large Language Models. *ACS Catalysis* **2023**, *13*, 16032–16044, Publisher: American Chemical Society.
- (39) Ock, J.; Meda, R. S.; Badrinarayanan, S.; Aluru, N. S.; Chandrasekhar, A.; Farimani, A. B. Large Language Model Agent for Modular Task Execution in Drug Discovery. 2025; <http://arxiv.org/abs/2507.02925>, arXiv:2507.02925 [cs].
- (40) Chaudhari, A.; Ock, J.; Farimani, A. B. Modular Large Language Model Agents for Multi-Task Computational Materials Science. 2025; <https://chemrxiv.org/engage/chemrxiv/article-details/681239c150018ac7c5d5accf>.
- (41) George, A.; Farimani, A. B. LLM Trainer: Automated Robotic Data Generating via Demonstration Augmentation using LLMs. 2025; <http://arxiv.org/abs/2509.20070>, arXiv:2509.20070 [cs].
- (42) Bartsch, A.; Farimani, A. B. LLM-Craft: Robotic Crafting of Elasto-Plastic Objects With Large Language Models. *IEEE Robotics and Automation Letters* **2025**, *10*, 10450–10457.
- (43) Chandrasekhar, A.; Farimani, A. B. Automating MD simulations for Proteins using Large language Models: NAMD-Agent. 2025; <http://arxiv.org/abs/2507.07887>, arXiv:2507.07887 [cs].
- (44) Merrill, C.; Raman, A.; George, A.; Barati Farimani, A. LLM-drone: aerial addi-

- tive manufacturing with drones planned using large language models. *Construction Robotics* **2025**, *9*, 20.
- (45) LangChain. <https://www.langchain.com>.
- (46) LlamaIndex - Build Knowledge Assistants over your Enterprise Data. <https://www.llamaindex.ai/>.
- (47) Anthropic Introducing the Model Context Protocol. 2024; <https://www.anthropic.com/news/model-context-protocol>.
- (48) Thermo-Calc Software Thermo-Calc Software. 2025; <https://thermocalc.com/>.
- (49) Akbari, P.; Zamani, M.; Mostafaei, A. Machine learning prediction of mechanical properties in metal additive manufacturing. *Additive Manufacturing* **2024**, *91*, 104320.
- (50) Lber, L.; Schimansky, F. P.; Khn, U.; Pyczak, F.; Eckert, J. Selective laser melting of a beta-solidifying TNM-B1 titanium aluminide alloy. *Journal of Materials Processing Technology* **2014**, *214*, 1852–1860.
- (51) Manfredi, D.; Calignano, F.; Krishnan, M.; Canali, R.; Ambrosio, E. P.; Atzeni, E. From Powders to Dense Metal Parts: Characterization of a Commercial AlSiMg Alloy Processed through Direct Metal Laser Sintering. *Materials* **2013**, *6*, 856–869, Publisher: Multidisciplinary Digital Publishing Institute.
- (52) Sun, G.; Zhou, R.; Lu, J.; Mazumder, J. Evaluation of defect density, microstructure, residual stress, elastic modulus, hardness and strength of laser-deposited AISI 4340 steel. *Acta Materialia* **2015**, *84*, 172–189.
- (53) Yadollahi, A.; Shamsaei, N.; Thompson, S. M.; Seely, D. W. Effects of process time interval and heat treatment on the mechanical and microstructural properties of direct laser deposited 316L stainless steel. *Materials Science and Engineering: A* **2015**, *644*, 171–183.

- (54) Kok, Y.; Tan, X. P.; Wang, P.; Nai, M. L. S.; Loh, N. H.; Liu, E.; Tor, S. B. Anisotropy and heterogeneity of microstructure and mechanical properties in metal additive manufacturing: A critical review. *Materials & Design* **2018**, *139*, 565–586.
- (55) Schmidtke, K.; Palm, F.; Hawkins, A.; Emmelmann, C. Process and Mechanical Properties: Applicability of a Scandium modified Al-alloy for Laser Additive Manufacturing. *Physics Procedia* **2011**, *12*, 369–374.
- (56) Hack, H.; Link, R.; Knudsen, E.; Baker, B.; Olig, S. Mechanical properties of additive manufactured nickel alloy 625. *Additive Manufacturing* **2017**, *14*, 105–115.
- (57) Rodriguez, O. L.; Allison, P. G.; Whittington, W. R.; Francis, D. K.; Rivera, O. G.; Chou, K.; Gong, X.; Butler, T. M.; Burroughs, J. F. Dynamic tensile behavior of electron beam additive manufactured Ti6Al4V. *Materials Science and Engineering: A* **2015**, *641*, 323–327.
- (58) Saunders, N.; Miodownik, P. The Application of CALPHAD Methods - ScienceDirect. <https://www.sciencedirect.com/science/article/abs/pii/S1470180498800308>.
- (59) Cross Plots for Alloy Design. 2023; <https://thermocalc.com/blog/icme-workflows-using-cross-plots-to-visualize-the-tradeoff-of-properties-in-alloy->
- (60) Property Model Calculator. <https://thermocalc.com/products/thermo-calc/property-model-calculator/>.
- (61) Bramson, M. A. *Infrared Radiation*; Springer US: Boston, MA, 1968.
- (62) Trapp, J.; Rubenchik, A. M.; Guss, G.; Matthews, M. J. In situ absorptivity measurements of metallic powders during laser powder-bed fusion additive manufacturing. *Applied Materials Today* **2017**, *9*, 341–349.

- (63) Nordet, G.; Gorny, C.; Mayi, Y.; Daligault, J.; Dal, M.; Effernelli, A.; Blanchet, E.; Coste, F.; Peyre, P. Absorptivity measurements during laser powder bed fusion of pure copper with a 1kW cw green laser. *Optics & Laser Technology* **2022**, *147*, 107612.
- (64) Cook, P. S.; Ritchie, D. J. Determining the laser absorptivity of Ti-6Al-4V during laser powder bed fusion by calibrated melt pool simulation. *Optics & Laser Technology* **2023**, *162*, 109247.
- (65) Honda, H.; Watanabe, M. Measurement of Laser Absorptivity of Inconel Powders with Additive Manufacturing Machine. *MATERIALS TRANSACTIONS* **2025**, *66*, 107–112.
- (66) Mills, K. Recommended Values of Thermophysical Properties for Selected Commercial Alloys. 2002; <http://www.sciencedirect.com:5070/book/monograph/9781855735699/recommended-values-of-thermophysical-properties-for-selected-commercial-alloys>, ISBN: 9781855735699.
- (67) He, X.; Kong, D.; Zhou, Y.; Wang, L.; Ni, X.; Zhang, L.; Wu, W.; Li, R.; Li, X.; Dong, C. Powder recycling effects on porosity development and mechanical properties of Hastelloy X alloy during laser powder bed fusion process. *Additive Manufacturing* **2022**, *55*, 102840.
- (68) Gordon, J. V.; Narra, S. P.; Cunningham, R. W.; Liu, H.; Chen, H.; Suter, R. M.; Beuth, J. L.; Rollett, A. D. Defect structure process maps for laser powder bed fusion additive manufacturing. *Additive Manufacturing* **2020**, *36*, 101552.
- (69) Ng, G. K. L.; Jarfors, A. E. W.; Bi, G.; Zheng, H. Y. Porosity formation and gas bubble retention in laser metal deposition. *Applied Physics A* **2009**, *97*, 641–649.
- (70) Bellini, C.; Berto, F.; Cocco, V. D.; Iacoviello, F.; Mocanu, L. P.; Razavi, N. Additive

- manufacturing processes for metals and effects of defects on mechanical strength: a review. *Procedia Structural Integrity* **2021**, *33*, 498–508.
- (71) Shrestha, S.; Chou, K. Formation of keyhole and lack of fusion pores during the laser powder bed fusion process. *Manufacturing Letters* **2022**, *32*, 19–23.
- (72) Smith, T. R.; Sugar, J. D.; Schoenung, J. M.; San Marchi, C. Relationship between manufacturing defects and fatigue properties of additive manufactured austenitic stainless steel. *Materials Science and Engineering: A* **2019**, *765*, 138268.
- (73) Pak, P.; Barati Farimani, A. AdditiveLLM: Large language models predict defects in metals additive manufacturing. *Additive Manufacturing Letters* **2025**, *14*, 100292.
- (74) Aboulkhair, N. T.; Maskery, I.; Tuck, C.; Ashcroft, I.; Everitt, N. M. On the formation of AlSi10Mg single tracks and layers in selective laser melting: Microstructure and nano-mechanical properties. *Journal of Materials Processing Technology* **2016**, *230*, 88–98.
- (75) Li, E.; Shen, H.; Wang, L.; Wang, G.; Zhou, Z. Laser shape variation influence on melt pool dynamics and solidification microstructure in laser powder bed fusion. *Additive Manufacturing Letters* **2023**, *6*, 100141.
- (76) Tapia, G.; Khairallah, S.; Matthews, M.; King, W. E.; Elwany, A. Gaussian process-based surrogate modeling framework for process planning in laser powder-bed fusion additive manufacturing of 316L stainless steel. *The International Journal of Advanced Manufacturing Technology* **2018**, *94*, 3591–3603.
- (77) Zhang, B.; Seede, R.; Xue, L.; Atli, K. C.; Zhang, C.; Whitt, A.; Karaman, I.; Arroyave, R.; Elwany, A. An efficient framework for printability assessment in Laser Powder Bed Fusion metal additive manufacturing. *Additive Manufacturing* **2021**, *46*, 102018.

- (78) Ki, H.; Mazumder, J.; Mohanty, P. S. Modeling of laser keyhole welding: Part I. mathematical modeling, numerical methodology, role of recoil pressure, multiple reflections, and free surface evolution. *Metallurgical and Materials Transactions A* **2002**, *33*, 1817–1830.
- (79) Gu, D.; Shen, Y. Balling phenomena during direct laser sintering of multi-component Cu-based metal powder. *Journal of Alloys and Compounds* **2007**, *432*, 163–166.
- (80) Lindström, V.; Lupo, G.; Yang, J.; Turlo, V.; Leinenbach, C. A simple scaling model for balling defect formation during laser powder bed fusion. *Additive Manufacturing* **2023**, *63*, 103431.
- (81) Anthropic Anthropic. 2025; <https://www.anthropic.com>.
- (82) modelcontextprotocol/python-sdk. 2025; <https://github.com/modelcontextprotocol/python-sdk>, original-date: 2024-09-24T21:01:35Z.
- (83) Ehtesham, A.; Singh, A.; Gupta, G. K.; Kumar, S. A survey of agent interoperability protocols: Model Context Protocol (MCP), Agent Communication Protocol (ACP), Agent-to-Agent Protocol (A2A), and Agent Network Protocol (ANP). 2025; <http://arxiv.org/abs/2505.02279>, arXiv:2505.02279 [cs].
- (84) Hou, X.; Zhao, Y.; Wang, S.; Wang, H. Model Context Protocol (MCP): Landscape, Security Threats, and Future Research Directions. 2025; <http://arxiv.org/abs/2503.23278>, arXiv:2503.23278 [cs].
- (85) Model context protocol (MCP) - OpenAI Agents SDK. <https://openai.github.io/openai-agents-python/mcp/>.
- (86) Hamsa Buvaraghan; Derek Egan MCP Toolbox for Databases (formerly Gen AI Toolbox for Databases) now supports Model Context Protocol (MCP).

2025; <https://cloud.google.com/blog/products/ai-machine-learning/mcp-toolbox-for-databases-now-supports-model-context-protocol>.

- (87) PyPI The Python Package Index. <https://pypi.org/>.
- (88) Subagents. <https://docs.anthropic.com/en/docs/claude-code/sub-agents>.
- (89) Claude 3.7 Sonnet and Claude Code. <https://www.anthropic.com/news/claude-3-7-sonnet>.
- (90) Introducing Claude 4. <https://www.anthropic.com/news/claude-4>.
- (91) Zhang, S.; Li, Y.; Dai, H.; Zhang, Z.; Chen, X. Achieving balanced uniform and local corrosion performance of SS 316L/IN625 hybrid alloy manufactured by directed energy deposition. *Journal of Materials Research and Technology* **2024**, *32*, 3937–3948.
- (92) Blkba, . S.; Serinda, T.; Grol, U.; Gnen, A.; am, G. Improving oxidation resistance of wire arc additive manufactured Inconel 625 Ni-based superalloy by pack aluminizing. *CIRP Journal of Manufacturing Science and Technology* **2023**, *46*, 89–97.
- (93) Fan, J.-k.; Yang, H.-c.; Zhang, P.-z.; Li, J.-y.; Jing, Z.-j.; Chen, F.-l.; Liu, D.-g.; Tang, B.; Kou, H.-c.; Li, J.-s. Mechanism of high temperature oxidation of Inconel 625 superalloy with various solution and ageing heat treatment processes. *Transactions of Nonferrous Metals Society of China* **2024**, *34*, 3662–3676.
- (94) Gonzalez, J. A.; Mireles, J.; Stafford, S. W.; Perez, M. A.; Terrazas, C. A.; Wicker, R. B. Characterization of Inconel 625 fabricated using powder-bed-based additive manufacturing technologies. *Journal of Materials Processing Technology* **2019**, *264*, 200–210.
- (95) Ahmed, N.; Barsoum, I.; Haidemenopoulos, G.; Al-Rub, R. K. A. Process parameter selection and optimization of laser powder bed fusion for 316L stainless steel: A review. *Journal of Manufacturing Processes* **2022**, *75*, 415–434.

- (96) Parikh, Y.; Kuttolamadom, M. Property-Graded Stainless Steel 316L by Selective Laser Melting: Characterization & Design. *Journal of Manufacturing Science and Engineering* **2023**, *145*.
- (97) Cacace, S.; Semeraro, Q. On the Lack of fusion porosity in L-PBF processes. *Procedia CIRP* **2022**, *112*, 352–357.
- (98) Pak, P.; Ogoke, F.; Polonsky, A.; Garland, A.; Bolintineanu, D. S.; Moser, D. R.; Arnhart, M.; Madison, J.; Ivanoff, T.; Mitchell, J.; Jared, B.; Salzbrenner, B.; Heiden, M. J.; Barati Farimani, A. ThermoPore: Predicting part porosity based on thermal images using deep learning. *Additive Manufacturing* **2024**, *95*, 104503.
- (99) Tucho, W. M.; Lysne, V. H.; Austb, H.; Sjolyst-Kverneland, A.; Hansen, V. Investigation of effects of process parameters on microstructure and hardness of SLM manufactured SS316L. *Journal of Alloys and Compounds* **2018**, *740*, 910–925.
- (100) Lu, P.; Cheng-Lin, Z.; Liang, W.; Tong, L.; Xiao-Cheng, L. Research on mechanical properties and microstructure by selective laser melting of 316L stainless steel. *Materials Research Express* **2020**, *6*, 1265h7, Publisher: IOP Publishing.
- (101) Chandrasekhar, A.; Chan, J.; Ogoke, F.; Ajenifujah, O.; Barati Farimani, A. AMGPT: A large language model for contextual querying in additive manufacturing. *Additive Manufacturing Letters* **2024**, *11*, 100232.
- (102) Akbari, P.; Ogoke, F.; Kao, N.-Y.; Meidani, K.; Yeh, C.-Y.; Lee, W.; Barati Farimani, A. MeltpoolNet: Melt pool characteristic prediction in Metal Additive Manufacturing using machine learning. *Additive Manufacturing* **2022**, *55*, 102817.